ORIGINAL ARTICLE

Hydrazone-linked soybean protein isolate-carboxymethyl cellulose conjugates for pH-responsive controlled release of pesticides

Guanghua Liu[1,2] · Guanquan Lin[3] · Mingyi Tan[3] · Hongjun Zhou[3] · Huayao Chen[3] · Hua Xu[3] · Xinhua Zhou[3]

Abstract

To improve the utilization of pesticides and reduce the amount of pesticides used, sustained-release nanoparticles were prepared. Soybean protein isolate (SPI) and carboxymethyl cellulose (CMC) were modified to obtain hydrazine-modified SPI and aldehyde-modified CMC, respectively, and SPI-CMC was prepared by the condensation of hydrazine and aldehyde groups, forming a hydrazone bond. SPI-CMC was heated and loaded with avermectin (AVM) to obtain AVM/SPI-CMC. The encapsulation efficiency property, anti-ultraviolet property, sustained-release characteristics, pH responsiveness, and toxicological profiles were studied. The particles in the formulation were spherical-like, with sizes ranging between 150 and 250 nm. The encapsulation efficiency increased with the addition of SPI, which reached 44.49% when SPI was added in a mass ratio of $m_{\text{SPI-HYD}}:m_{\text{CMC-ALD}} = 2{:}1$. The percentage of remaining AVM in AVM/SPI-CMC was 31.47% higher than that in the AVM solution after UV irradiation for 43 h. Moreover, the nanoparticles were responsive to pH. SPI-CMC had no significant effect on the insecticidal toxicity of AVM. Environmental friendly SPI-CMC could protect and release pesticides continuously, which could improve the efficiency of pesticides.

Introduction

Recently developed agricultural practices are largely dependent on the use of pesticides. Pesticides can reduce agricultural losses by 30–40% [1, 2]. However, conventional pesticide formulations possess various disadvantages, e.g., a high content of organic solvents, poor dispersibility, dust drift and high toxicity [3, 4]. These conventional formulations, owing to their low-targeting efficiency (less than 1%), contain components that contaminate the soil and water, thus endangering human health [5]. Nanopesticide formulations [6], such as nanoemulsions, nanocapsules, nanosuspensions, and nanoparticles [7–9], can significantly improve the utilization rate of pesticides due to their small particle sizes, high specific surface areas, good stability, dispersibility, and mobility, and the resulting formulations are sustainable. In addition, nanopesticide formulations are safer and more economical than conventional formulations [10]. Zou et al. [11] employed template-free methods to prepare polydopamine (PDA) particles and encapsulated lambda-cyhalothrin (LC) to obtain LC-loaded PDA microcapsules. These microcapsules exhibited a spherical shape at the nanometer scale and displayed a sustained-release property, which, in turn, improved the long-term effectiveness of the pesticides. Li et al. [12] utilized sodium lignosulfonate (SL) and cetyltrimethylammonium (CTAB) to self-assemble and encapsulate avermectin (AVM) to finally obtain AVM@SL-CTAB microspheres. These microspheres increased the half-life of AVM by 7.5 times under UV light, thus demonstrating the sustained-release property and improving the utilization rate of the pesticides.

Stimulus-responsive drug-release technology can accurately release pesticides in response to some environmental changes, thus improving the efficiency of a pesticide. A hydrazone bond (HYD) is a pH-responsive molecular bond

✉ Hongjun Zhou
  hongjunzhou@163.com

✉ Xinhua Zhou
  cexinhuazhou@163.com

1 School of Agriculture and Biology, Zhongkai University of Agriculture and Engineering, Guangzhou, P. R. China

2 Shaoguan Huashi Innovational Research Institute for Modern Agriculture, Shaoguan, P. R. China

3 Key Laboratory of Agricultural Green Fine Chemicals of Guangdong Higher Education Institution, School of Chemistry and Chemical Engineering, Zhongkai University of Agriculture and Engineering, Guangzhou, P. R. China

that breaks down in acidic environments and is stable in neutral and alkaline conditions [13, 14]. Therefore, a HYD can be used make any pesticide carrier responsive to pH. Qi et al. [15] prepared mPEG-HYD-PCL by connecting polyethylene glycol (PEG) and polycaprolactone (PCL) through a HYD and PTX-loaded PEG-Hyd-PCL micelles were obtained by encapsulating paclitaxel (PTX) via self-assembly. The release rate of PTX from the micelles was faster in acidic conditions than in neutral or basic conditions. Jiang et al. [16] utilized poly(ethylene glycol) monomethyl ether (mPEG), 5-allyloxy-1,3-dioxan-2-one (ATMC), and 2,2-dimethyltrimethylene carbonate (DTC) to synthesize the amphiphilic block copolymer mPEG-b-P(ATMC-co-DTC). Doxorubicin (DOX) was covalently conjugated to mPEG-b-P(ATMC-co-DTC) through a HYD to obtain mPEG-b-P(ATMC-co-DTC)-graft-DOX (mPEG-*b*-P(ATMC-*co*-DTC)-*g*-DOX). The samples showed that the HYDs were broken at a pH of 5, resulting in the rapid release of DOX.

Soybean protein isolate (SPI) [17] is a naturally sourced plant protein that is biodegradable and nontoxic, and is an environmental friendly solution that can be used to prepare nanopesticide formulations. After thermal denaturation, the hydrophobic groups of SPI are exposed, and their hydrophobic property is enhanced [18], which is preferable for encapsulating hydrophobic pesticides. However, the SPI becomes unstable after heating, and the SPI coagulates. Carboxymethyl cellulose (CMC) [19] is a water-soluble polyanionic cellulose compound that is inexpensive and widely available. CMC has good thickening and water retaining properties and is biodegradable, biocompatible and nontoxic, and therefore, it can be used as a stabilizer. In this work, SPI was modified with CMC to improve the stability and dispersibility of SPI. Moreover, SPI was rendered pH-responsive by linking SPI and CMC through a HYD. After heating the carrier and encapsulating the pesticide, the encapsulation efficiency, anti-UV properties, responsiveness to stimuli, and toxicological effect of the formulations were studied. The outcomes of this study will encourage the application of SPI to further develop many stimulus-responsive nanocarriers of pesticides in the future. In addition, the use of biodegradable protein and cellulose to prepare nanopesticide carriers could avoid the use of nondegradable materials and improve the safety of materials, which is conducive for developing agriculture in a manner that is not harmful to human health.

Materials and methods

Materials

SPI was obtained from defatted soybean powder (Anhui Suzhiwei Shengwu Co., Ltd.) [20]. The defatted soybean powder was soluble in water, the pH was adjusted to 7.5, and an insoluble substance was filtered by centrifugation. The pH of the filtrate was adjusted to 4.5, and the filtrate was centrifuged to obtain the filtrate residue. Finally, the pH of the system was adjusted to 7.0, and the SPI was obtained by lyophilization after dialysis (cut-off molecular weight: 14,000 Da) was performed for 24 h. The CMC (90 kDa) and sodium periodate were purchased from Aladdin Reagent Co., Ltd. Ethanol, methanol, hydrochloric acid (HCl), ethylene glycol, and hydrazine hydrate were obtained from Tianjin Damao Chemical Reagents. The abovementioned reagents were pure analytical grade reagents. AVM (purity ≥ 95%) was obtained from Hebei Weiyuan Biochemical Co., Ltd.

Preparation of hydrazone-modified SPI (SPI-HYD)

In a typical procedure, 3.0 g SPI was dispersed in 100 mL methanol using a three-necked flask, and then, the suspension was mixed by magnetic stirring at 25 °C. Approximately, 4.2 mL HCl (1 mol/L) was added dropwise to the suspension. The reaction was allowed to proceed for 6 h while maintaining a constant temperature. The esterified SPI powder was obtained by removing the solvent at 40 °C [21]. The esterified SPI powder was then suspended in 50 mL methanol. Then, 10 mL hydrazine hydrate was added dropwise to the suspension with constant stirring at 25 °C, and the reaction was allowed to proceed for 24 h. Subsequently, the mixture was subjected to dialysis while the pH was maintained at 4.3. The mixture was then vacuum filtered and freeze-dried to prepare SPI-HYD.

Preparation of aldehyde-modified CMC (CMC-ALD)

Approximately, 5.0 g CMC was mixed with 200 mL deionized water, and the pH was adjusted to 5.0 until the entire amount of the CMC was dissolved. Approximately, 5.0 g sodium periodate was dissolved in 50 mL deionized water. Under dark conditions, the sodium periodate solution was added dropwise into the CMC solution, and the resulting solution was magnetically stirred for 24 h at 25 °C. After that, 5 mL ethylene glycol was added dropwise into the mixed solution, and this solution was magnetically stirred for 1 h at 25 °C in the dark to deactivate any unreacted periodate. Finally, the sample was dialyzed and lyophilized to obtain the CMC-ALD powder.

Preparation of SPI-CMC and AVM/SPI-CMC

Approximately, 1.0 g each of SPI-HYD and CMC-ALD was dissolved in a phosphate buffer (pH = 7.4). The mixture was then magnetically stirred at 45 °C for 3 h, and the SPI-CMC powder was obtained after the mixture was dialyzed and freeze-dried. A flowchart describing the preparation process is shown in Fig. 1. Approximately, 0.5 g SPI-CMC was added to a beaker and dissolved in 90 mL
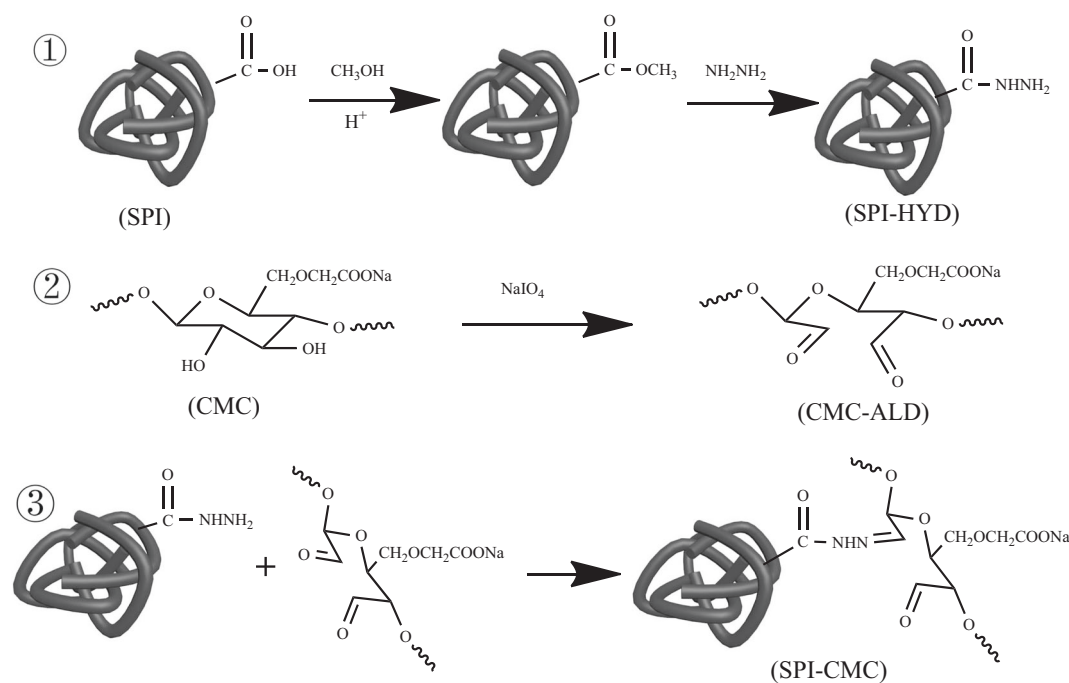
Fig. 1 Schematic representation of the syntheses of SPI-CMC

deionized water. Separately, AVM was dissolved in ethanol to prepare a 10 mg/mL solution. Next, the SPI-CMC solution was mixed with 2 mL AVM-ethanol solution, and the resulting solution was stirred for 1 h at 80 °C. After cooling, the volume of the solution was increased to 100 mL with deionized water to obtain AVM/SPI-CMC.

Characterization of AVM/SPI-CMC

Proton nuclear magnetic resonance

^{1}H NMR spectra of CMC and CMC-ALD in D_2O were measured on an Ascend 400 MHz spectrometer (Bruker Analytical Instruments, USA) at room temperature.

Fourier transform infrared spectroscopy

CMC, CMC-ALD, SPI, SPI-HYD, SPI-CMC, and AVM/SPI-CMC were analyzed using Spectrum 100 Fourier transformed infrared spectrometry (PerkinElmer Inc., USA) in the range of 4000–450 cm^{-1}.

Thermo gravimetric analyzer

The thermal decomposition of CMC, CMC-ALD, SPI, SPI-HYD, and SPI-CMC was measured by a thermo gravimetric analyzer 2 (TGA2) (Mettler Toledo, Switzerland). A nitrogen flow of 20 mL/min and a temperature range of 40–600 °C were used in the TGA method. The heating rate used was always 10 °C/min.

Scanning electron microscope

The SPI-CMC and AVM/SPI-CMC solutions were deposited onto a sample stage, dried naturally and sputtered with gold nanoparticles for 45 s [22]. The morphologies of SPI-CMC and AVM/SPI-CMC were observed using an S-4800 scanning electron microscope (SEM) (Hitachi, Japan) at 5.0 kV under nitrogen.

Particle size and zeta potential

The samples were diluted by 100-fold. Then, the resulting sample solutions (pH = 7) were added to sample cells and ultrasonically dispersed for 5 min. A 90Plus PALS dynamic light scattering instrument (Brookhaven Analytical Instruments, USA) was employed to study the SPI, SPI-CMC, and AVM/SPI-CMC solutions. The samples were diluted by 100-fold. Then, the resulting sample solutions were added to sample cells and ultrasonically dispersed for 5 min. The zeta potentials of the samples (pH = 7) were measure by the 90Plus PALS dynamic light scattering instrument after the test electrode was inserted into the sample cell.

Encapsulation efficiency test

The encapsulation efficiency of AVM was tested by a high-speed centrifuge (TGL-16G, Anting Scientific Instrument, China). Approximately, 4 mL AVM/SPI-CMC was centrifuged at an RCF of 9982g (12,000 r/min) for 30 min. After that, 1 mL supernatant solution was

removed by a pipette and diluted to 25 mL with ethanol. The absorbance of the dilute supernatant solution was measured by a UV-2550 UV spectrophotometer (Shimadzu, Japan) ($\lambda = 245$ nm, $A = 0.0377C - 0.0315$; $R^2 = 0.9908$). The mass of the unencapsulated AVM ($m_{\text{free AVM}}$) was calculated from the standard curve. The encapsulation efficiency was obtained according to Eq. (1).

$$EE\ (\%) = (m_{\text{total AVM}} - m_{\text{free AVM}})/m_{\text{total AVM}} \times 100\ \%. \tag{1}$$

Anti-UV property test

The concentration of AVM in each 100 mL test sample (the AVM-ethanol solution and AVM/SPI-CMC) was fixed at 0.2 mg/mL. Both the AVM/SPI-CMC and AVM-ethanol solutions were placed 20 cm away from a 16 W UV lamp. After irradiating the sample solution for a time i, 1 mL sample solution was removed by a pipette and diluted to 25 mL with ethanol. A 0.22 μm filter membrane was used to filter the diluted sample. Then, the absorbance A_i of AVM was measured using a UV spectrophotometer, and the remaining ratio (RR) of AVM was obtained according to Eq. (2).

$$RR = A_i/A_0, \tag{2}$$

where A_0 is the absorbance of AVM at time 0.

Sustained-release property test

The sustained-release experiment was performed according to a method described by Lin et al. [18]. The standard curve obtained for the sustained release was $A = 0.0305C - 0.0014$ with $R^2 = 0.9992$. The concentration of AVM (ρ_i) could be calculated from the standard curve. The cumulative release rate (R_i) [23] was obtained according to Eq. (3).

$$R_i = \begin{cases} \rho_i \times 0.05/m_{\text{AVM}} & (i = 1) \\ \rho_i \times 0.05/m_{\text{AVM}} + \sum_{i=1}^{i-1} \rho_i \times 0.001/m_{\text{AVM}} & (i = 2,\ 3,\ 4...) \end{cases} \tag{3}$$

Difference analysis

The probability (P) of the intergroup difference was determined by performing an analysis of covariance (ANCOVA) using SPSS software (Chicago, IL, USA). The model-independent method was adopted to analyze the curve differences. The difference factor (f_1) was obtained using Eq. (4), and the similarity factor (f_2) [24] was obtained using Eq. (5).

$$f_1 = 100 \left(\frac{\sum_{t=1}^{n} |R_t - T_t|}{\sum_{t=1}^{n} R_t} \right), \tag{4}$$

$$f_2 = 50 \log \left\{ \left[\left(1 + \left(\frac{1}{n} \right) \sum_{t=1}^{n} (R_t - T_t)^2 \right) \right]^{-0.5} \times 100 \right\}, \tag{5}$$

where R_t represents the R_i of the reference sample at time t, and T_t represents the R_i of the test sample at time t.

Toxicity profile test

Insecticidal experiments were performed according to a method described by Chen et al. [23]. Leaves were treated by a soaking method and then fed to diamondback moths. The number of dead diamondback moths was observed after 48 h.

Results and discussion

¹H NMR analysis

Figure 2a shows the ¹H NMR spectra of CMC and CMC-ALD. For the CMC spectra, the δ signal between 3 and 5 ppm was due to the C–H and O–H groups of the CMC backbone. For the CMC-ALD spectra, a new signal appeared at 8.39 ppm, which was assigned to the –CHO group [25], indicating that CMC-ALD has been successfully prepared.

FTIR analysis

Figure 2b shows the Fourier transform infrared spectroscopy (FTIR) spectra of CMC, CMC-ALD, SPI, SPI-HYD, SPI-CMC, AVM/SPI-CMC, and AVM. The strong signal at 1604 cm⁻¹ observed in the CMC spectrum was attributed to the conjugate stretching vibration of O–C–O in carboxylate groups. The signal at 1329 cm⁻¹ corresponded to a −OH bending vibration. A new peak appeared in the CMC-ALD spectrum at 1730 cm⁻¹, which was ascribed to the C = O stretching vibration [26]. These results indicated that sodium periodate successfully broke the bond between C-2 and C-3 of the CMC and oxidized C–OH to form C = O [27]. The peak at 1654 cm⁻¹ in the SPI spectrum indicated the stretching vibration of –C = O in –CONH– (denoted as amide absorption band I). The peak at 1536 cm⁻¹ was

a

b
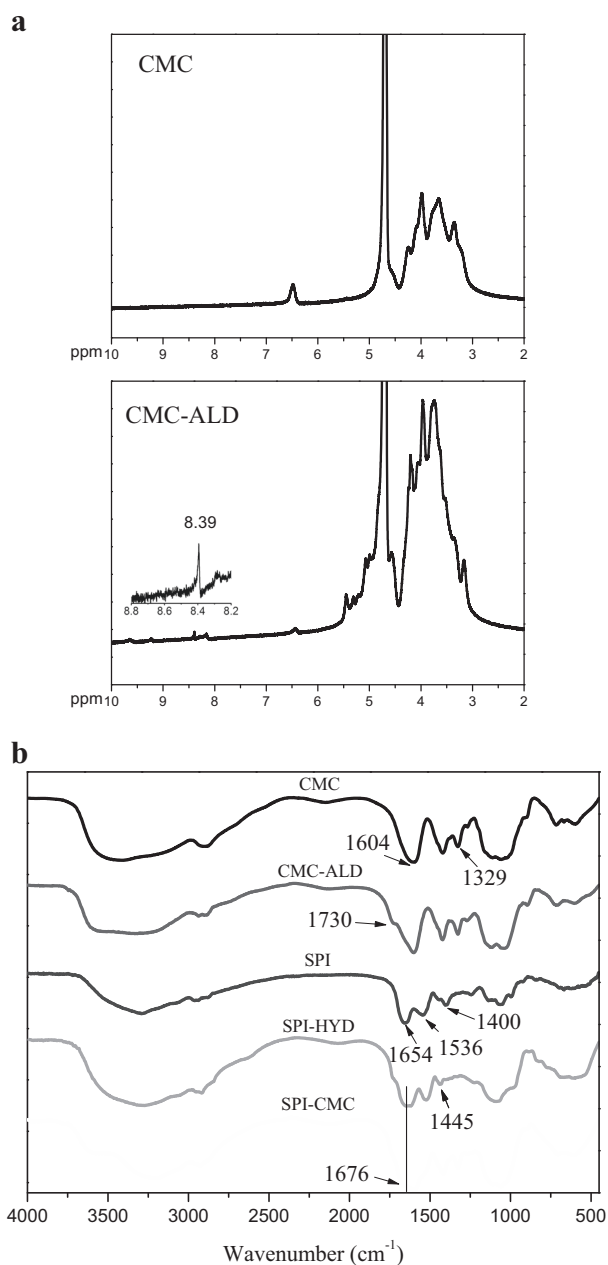
Fig. 2 **a** ^{1}H NMR spectra of CMC and CMC-ALD. **b** FTIR spectra of CMC, CMC-ALD, SPI, SPI-HYD, and SPI-CMC

ascribed to the coupling of the N–H bending vibration and C–N stretching vibration (denoted as amide absorption band II). A new peak appeared at 1445 cm^{-1} in the SPI-HYD spectrum, which belonged to the stretching vibration of N–H in the hydrazone group. The absorption peak at 1654 cm^{-1} broadened as the peaks corresponding to the bending vibration of –NH– in the hydrazone group and the stretching vibration of C = O overlapped. In addition, a peak at 1400 cm^{-1}, which was attributed to the stretching vibration of C–O^{-} in the carboxylate group [28], disappeared. This phenomenon suggested that the SPI was

successfully modified by hydrazine hydrate. A new peak appeared at 1676 cm^{-1} in the SPI-CMC spectrum, which was ascribed to the C = N stretching vibration. The characteristic peaks of CMC and SPI at 1604, 1329, 1654, and 1536 cm^{-1} were observed. In addition, the absorption peak corresponding to CMC-ALD at 1730 cm^{-1} and SPI-HYD at 1445 cm^{-1} disappeared, indicating that the reaction between the hydrazine and aldehyde groups was successful.

TGA analysis

Figure 3 shows the TGA (a, c, and e) and DTG (b, d, and f) thermograms of CMC, CMC-ALD, SPI, SPI-HYD, and SPI-CMC. Figure 3a shows that CMC started to decompose at 280 °C, and after modification, the initial decomposition temperature decreased to 150 °C. To further investigate these weightless steps, the DTG results of CMC and CMC-ALD were studied. Figure 3b shows that a decomposition peak appeared at 296 °C. Compared to the thermogram obtained for CMC, the peak intensity at 296 °C decreased, and two new decomposition peaks appeared at 160 and 220 °C. These results suggest that the ring structure of CMC opened, and then, aldehyde groups formed [29–31]. Figure 3c shows that the SPI started to decompose at 213 °C, and the initial decomposition temperature of SPI-HYD was 288 °C. Figure 3d shows that, when SPI-HYD was generated by the SPI, the peak corresponding to the original decomposition temperature at 290 °C shifted to 305 °C. As shown in Fig. 3f, the DTG thermogram of SPI-CMC indicated that the peak corresponding to the decomposition of SPI-CMC at 160 °C was the same as that of CMC-ALD. The peak at 220 °C may be attributed to the aldehyde group, and this peak disappeared or shifted to 248 °C. The peaks attributed to the decomposition of SPI-HYD at 233 and 305 °C shifted to 248 and 313 °C, respectively, in the SPI-CMC thermogram, indicating that the reaction between SPI-HYD and CMC-ALD successfully improved their respective stabilities.

SEM analysis

Figure 4 shows SEM images of (a) SPI-CMC and (b) AVM/SPI-CMC. Figure 4a shows that the size of the SPI-CMC particles was between 100 and 200 nm. The SPI-CMC particles had irregular shapes, as the tertiary and quaternary structures of the SPI determined the shape and size of the resulting particles. The carboxyl groups on the surface of CMC were responsible for homogeneously dispersing the particles through electrostatic repulsions. As shown in Fig. 4b, AVM/SPI-CMC exhibited particle sizes between 150 and 250 nm, and the resulting particles were spherical. After the loading of AVM, the particle size increased, as ethanol destroyed the hydration layer on the surface of
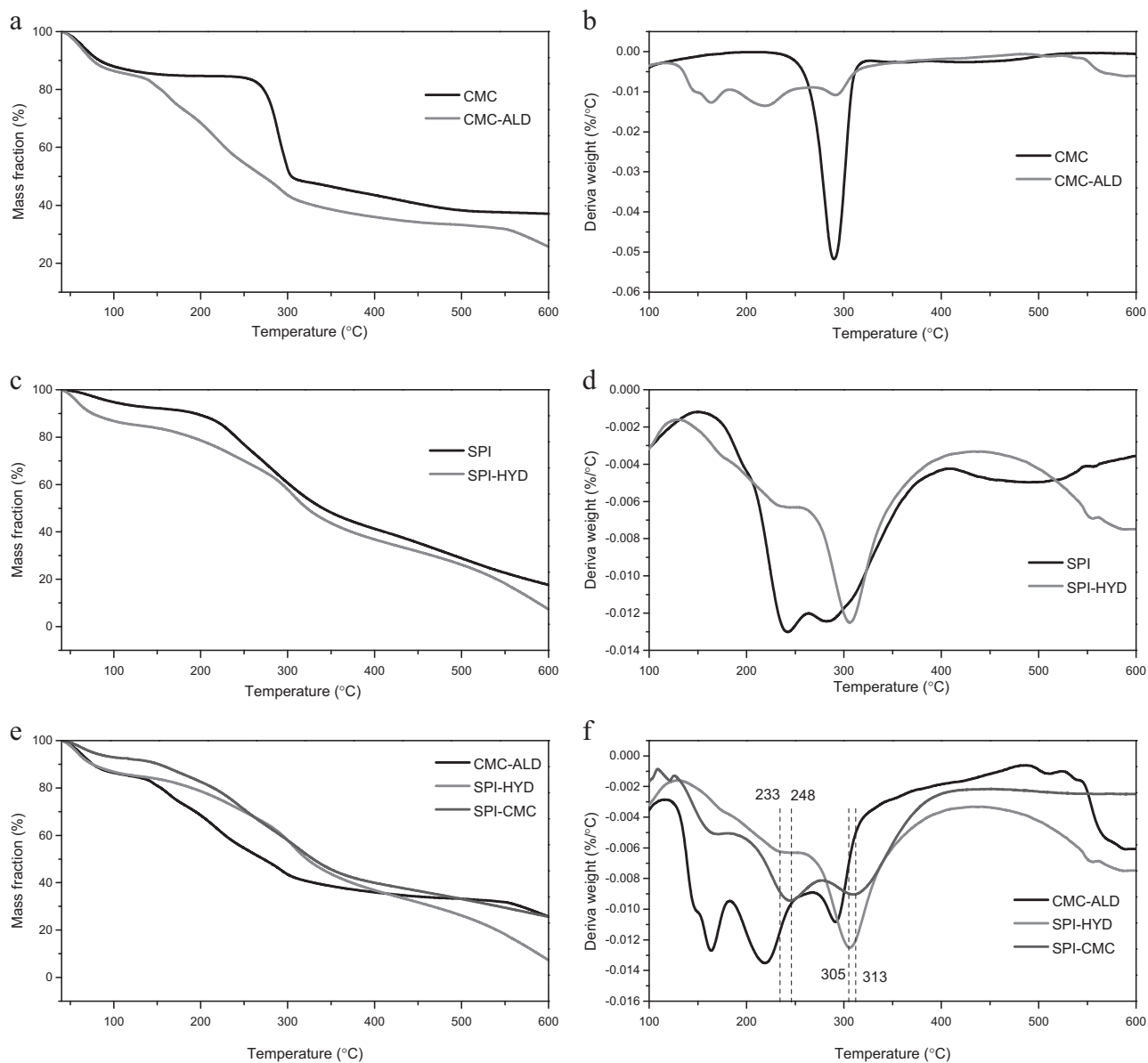
Fig. 3 TGA and DTG thermograms of **a**, **b** CMC, CMC-ALD, **c**, **d** SPI, SPI-HYD, and **e**, **f** SPI-CMC

Fig. 4 SEM images of **a** SPI-CMC and **b** AVM/SPI-CMC
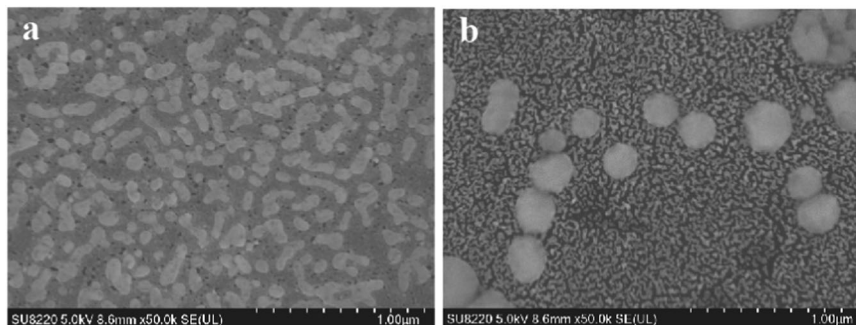
SPI-CMC and reduced the surface charge, leading SPI-CMC to aggregate and increase its particle size.

Simultaneously, the carboxyl group on the surface might exert an anti-aggregation effect, and thus, the particles could

Table 1 Average particle size and zeta potential of SPI and SPI-CMC

Sample	Average particle size (nm)	Zeta potential (mV)
SPI	160.35	−14.28
SPI (upon heating)	–	−8.73
SPI-CMC ($m_{SPI-HYD}$:$m_{CMC-ALD}$ = 2:1)	177.82	−27.19
SPI-CMC ($m_{SPI-HYD}$:$m_{CMC-ALD}$ = 1:1)	151.39	−30.07
SPI-CMC ($m_{SPI-HYD}$:$m_{CMC-ALD}$ = 1:2)	143.02	−39.94

Table 2 Effect of the mass ratio on the encapsulation efficiency, average particle size and zeta potential of AVM/SPI-CMC

$m_{SPI-HYD}$: $m_{CMC-ALD}$	Encapsulation efficiency (%)	Average particle size (nm)	Zeta potential (mV)
2:1	44.49	226.87	−18.37
1:1	39.94	185.74	−20.76
1:2	32.04	154.53	−29.63

remain dispersed, even when the particle size increased to a certain value. In addition, when the SPI was thermally denatured, the hydrophobic group of the SPI rotated outward, which enhanced the hydrophobicity of the resulting particle. Thus, the hydrophobic group could induce AVM to encapsulate, increasing the particle size.

Analysis of the zeta (ζ) potential and average particle size

As shown in Table 1, after heating, the SPI particle size of 160.35 nm increased as precipitates formed due to thermal aggregation, and the negative surface charge decreased from −14.28 to −8.73. SPI could not be loaded directly into the hydrophobic AVM due to its instability after heating. Thus, SPI should be modified with CMC to improve its stability. The average particle size of SPI-CMC decreased, and the negative surface charge increased with an increase in the CMC mass ratio. As the mass ratio of CMC increased, the number of carboxyl groups in SPI-CMC and the negative charge on the surface also increased, which, in fact, reduced the aggregation of particles and led to smaller particle sizes.

Analysis of the encapsulation efficiency

Table 2 shows that the encapsulation efficiency also increased with an increase in the mass ratio of SPI. As AVM was encapsulated mainly by SPI, the number of AVM carriers increased with an increase in the mass ratio of SPI, which led to an increase in the number of hydrophobic groups and a higher encapsulation efficiency. The particle size increased after AVM was loaded into SPI-CMC. This phenomenon occurred after the addition of organic solvents, which reduced the dielectric constant of the surface [32]; as a result, some of the particles aggregated, and the particle size increased. On the other hand, the thermal denaturation of SPI and encapsulation of AVM also increased the particle size. The negative charge increased with an increase in the mass ratio of CMC-ALD, which was mainly caused by the increase in the number of carboxyl groups. In addition,

in contrast to the results shown in Tables 1 and 2 show that the negative surface charge of the loaded drug decreased because the ethanol solvent in the AVM solution shielded part of the charge, resulting in a decrease in the negative surface charge.

Evaluation of the anti-UV property

According to previous reports, when exposed to UV radiation, the structure of AVM is unstable and decomposes [33]. Herein, we aimed at reducing the environmental impact on AVM and improving its stability. Figure 5 shows the percentage of undecomposed AVM that remained after UV-induced degradation. After 3 h of irradiation, the remaining ratio of AVM in the AVM solution was 76.82%, while after 19 h of irradiation, the remaining ratio was only 43.93%. For AVM/SPI-CMC ($m_{SPI-HYD}$:$m_{CMC-ALD}$ = 2:1), the remaining ratio of AVM was 81.08% and 79.02% after 3 and 19 h of irradiation, respectively. After loading SPI-CMC, the stability of AVM improved remarkably because SPI-CMC acted as a physical barrier, which could refract or absorb some UV light and prevent the direct exposure of AVM to the UV irradiation [34]. At the same time, CMC contained chromophores such as carboxyl and hydroxyl groups, which could absorb some UV light and slow the decomposition of AVM [35].

Evaluation of the sustained-release property

Figure 6a shows the effect of SPI-CMC on the sustained-release properties at a pH of 7 and at different mass ratios. During the first 4 h, AVM was released rapidly, and the cumulative release rates of AVM/SPI-CMC ($m_{SPI-HYD}$:$m_{CMC-ALD}$ = 2:1), AVM/SPI-CMC ($m_{SPI-HYD}$:$m_{CMC-ALD}$ = 1:1), and AVM/SPI-CMC ($m_{SPI-HYD}$:$m_{CMC-ALD}$ = 1:2) reached 51.27%, 56.85%, and 70.09%, respectively, which were similar to the ratio of unencapsulated AVM relative to the encapsulation efficiency, as shown in Table 2. Thus, AVM that was not encapsulated or did not attach to the surface of the drug-loaded particles was quickly released, resulting in a sudden increase in the cumulative release rate [36, 37]. After 170 h, the release of AVM reached steady-state, and the cumulative release rates of AVM/SPI-CMC ($m_{SPI-HYD}$:$m_{CMC-ALD}$ = 2:1),
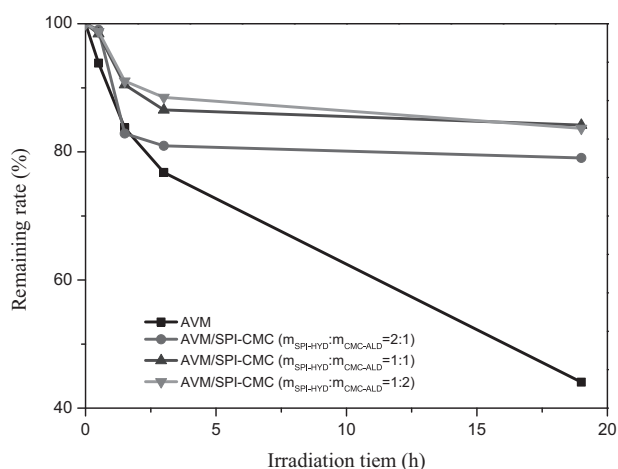
Fig. 5 Remaining ratio of AVM after UV irradiation
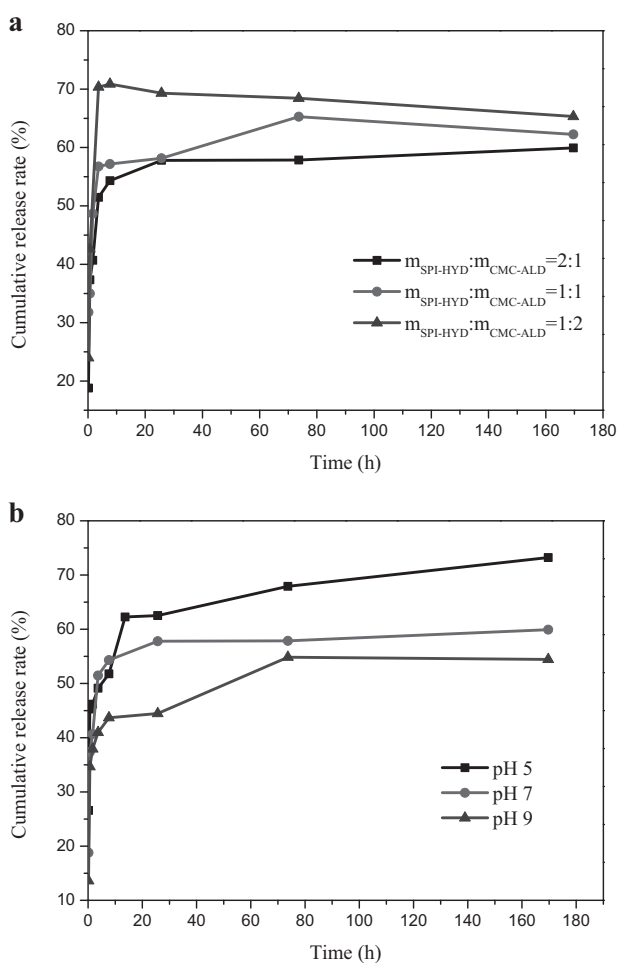
Fig. 6 Effects of **a** the mass ratio of SPI-HYD and CMC-ALD and **b** the pH on the sustained-release of AVM

increase in the SPI mass ratio, as AVM entered SPI via hydrophobic effects. When the SPI mass increased, the number of hydrophobic groups also increased, enhancing the hydrophobic effect, and as a result, the release rate of AVM decreased.

Figure 6b shows the sustained-release performance of AVM/SPI-CMC ($m_{SPI-HYD}$:$m_{CMC-ALD}$ = 1:1) at different pH values. When the release of AMV reached steady-state, the cumulative release rate at a pH of 5 was approximately 15% greater than that observed at a pH of 7, while the cumulative release rate at a pH of 9 was the lowest. Under acidic conditions, the HYD that connected SPI to CMC was broken [38], causing SPI to easily aggregate without the stabilizing effect of CMC, and the release of AVM was accelerated. At a pH of 7, the zeta potential of SPI (upon heating) was only −8.73 mV. When the pH was 5, the pH was close to the isoelectric point of SPI, which would reduce the surface charge of SPI. Therefore, the stability of SPI decreased, and the release of AVM accelerated. Under alkaline conditions, the HYD did not break, and the carboxyl groups of CMC mainly existed in the form of carboxylic acid ions, which could improve the stability and slow the release of AVM. Therefore, adjusting the pH could effectively control the drug release.
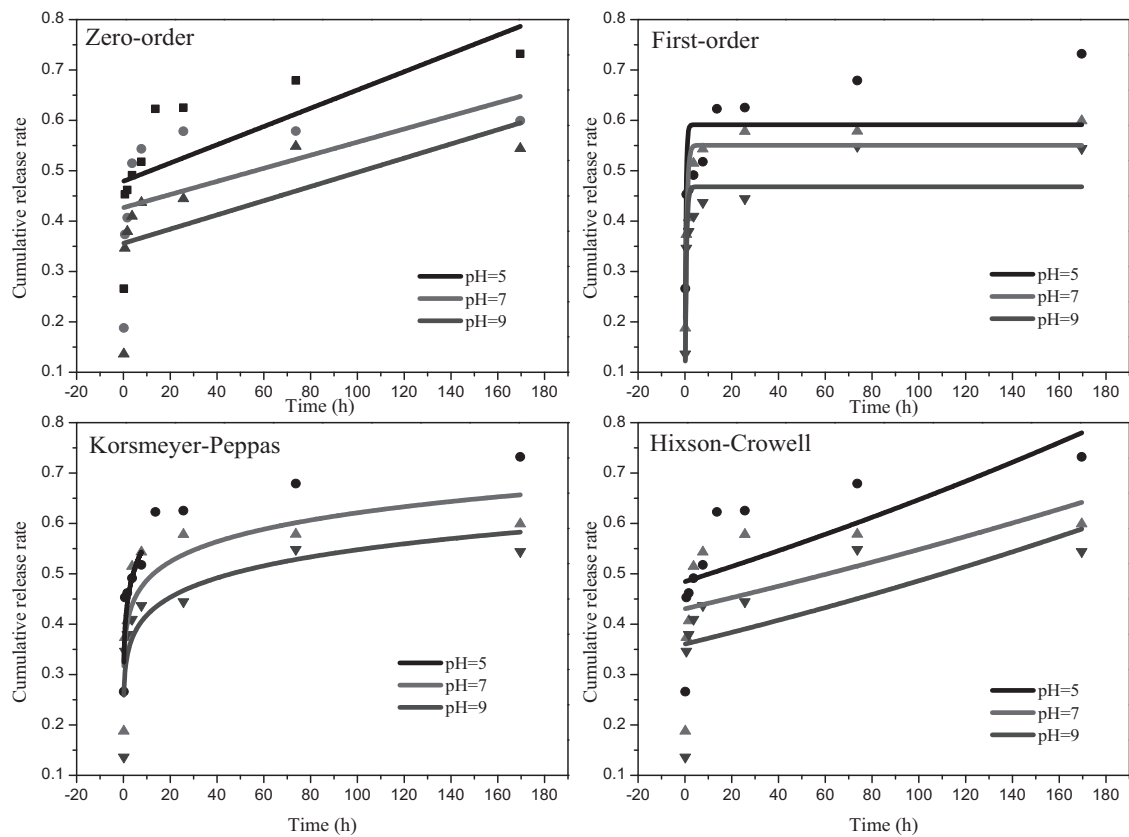
Kinetic studies

Zero-order [39], first-order [40, 41], Korsmeyer-Peppas [42, 43], and Hixson-Crowell [44, 45] models were used to fit the data of the curves obtained at pH values of 5, 7, and 9 to further study the release mechanism. The model fitting diagram and the fitting results are shown in Fig. 7 and Table 3, respectively. According to the correlation coefficient (R), the sustained-release data were consistent with the Korsmeyer-Peppas model. When the pH was 5, 7, and 9, the dispersion coefficients (n) were 0.4236, 0.3819, and 0.3187, respectively (all these values were less than 0.45). Thus, AVM was released from SPI-CMC by Fickian diffusion [46–48]. In addition, the difference in the concentration considerably influenced the release process [49]. It was found that, as the pH decreased from 9 to 5, n was closer to 0.45, which indicated that the release of AVM from SPI-CMC occurred by non-Fickian diffusion. This may occur due to the breaking of the HYD and because the pH was close to the isoelectric point of the SPI, leading to a decrease in the surface charge and the aggregation of the SPI. If the pH of the system is further lowered to the isoelectric point, SPI-CMC may precipitate and release AVM.

Difference analysis of the sustained-release curves

We evaluated the influence of the pH on the sustained-release curves by analyzing the sustained-release data using

AVM/SPI-CMC ($m_{SPI-HYD}$:$m_{CMC-ALD}$ = 1:1), and AVM/SPI-CMC ($m_{SPI-HYD}$:$m_{CMC-ALD}$ = 1:2) were 59.59%, 62.31% and 65.58%, respectively. When the release of AVM reached steady-state, the cumulative release rate decreased with an

Fig. 7 Model fitting for the sustained-release curves obtained at various pH values

Table 3 Fitting results of the sustained-release curves obtained at various pH values

Kinetic model	pH	c_1	c_2	R^2
Zero-order	5	0.0018	0.47903	0.4441
	7	0.0013	0.4267	0.1840
	9	0.0014	0.3559	0.3188
First-order	5	2.5198	0.5911	0.5482
	7	1.5125	0.5506	0.7635
	9	1.7810	0.4681	0.7851
Korsmeyer-Peppas	5	0.4236	0.1134	0.9085
	7	0.3819	0.1056	0.7275
	9	0.3187	0.1176	0.7708
Hixson-Crowell	5	0.7854	−7.9626	0.4171
	7	0.7551	−6.3369	0.1669
	9	0.7117	−7.4536	0.2933

Table 4 Results of the statistical analysis

Reference sample	Control sample	f_1	f_2	P
pH = 5	pH 7	12.82	55.68	0.457
	pH 9	23.20	44.40	0.101

the model-independent method. The curve obtained at pH values of 7 and 9 were compared with those obtained at a pH of 5. The results of f_1 and f_2 are shown in Table 4. For f_1 values up to 15 and f_2 values over 50, the difference between the two curves was less than 10%. This showed that the two curves had systematic similarities [50, 51]. The comparison of the curves obtained at pH values of 5 and pH 7 showed that f_1 was less than 15, while f_2 was above 50. This result indicated that these curves were very similar, and the difference was not significant. The curves obtained at pH values of 5 and 9 were compared, and $P = 0.101$, which was higher than the critical statistical value ($p = 0.05$), indicating that there was no significant difference between the two curves. However, $f_1 = 23.20$, which was higher than 15, and $f_2 = 44.40$, which was lower than 50. These results showed that the two curves had no systematic similarity. Therefore, as the pH increases, the difference between the sustained-release curves also increases.

Toxicity study

We investigated the insecticidal effects of AVM before and after loading, along with its toxicity. Table 5 shows the

Table 5 Insecticidal results of AVM and AVM/SPI-CMC

Sample	Toxicological regression equation	LC_{50} (mg/L)	95% confidence interval	R^2
AVM	$Y = 3.3207 + 0.9663\times$	54.69	33.67–88.85	0.9107
AVM/SPI-CMC	$Y = 3.7547 + 0.5426\times$	197.36	44.93–866.86	0.9515

results of the insecticidal analysis. The 95% confidence interval calculated for AVM in the original drug formulation was between 33.67 and 88.85. The probability of being outside this range was only 5%, indicating a significant difference in the insecticidal toxicity before and after loading with AVM. After AVM was encapsulated by SPI-CMC, the LC_{50} was increased from 54.69 to 197.36 mg/L, but the 95% confidence interval of AVM/SPI-CMC was not completely outside the 95% confidence limit interval of AVM in the original drug formulation. Therefore, after SPI-CMC encapsulated AVM, the insecticidal effect of AVM was not significantly changed.

Conclusions

SPI was bonded to CMC by a hydrazine bond to prepare SPI-CMC carriers for pesticide applications. AVM/SPI-CMC was obtained by encapsulating AVM with SPI-CMC through thermal denaturation. After the encapsulation of AVM, the anti-UV properties were markedly improved, and the decomposition rate was significantly reduced, resulting in a prolonged half-life. The sustained-release of AVM could be controlled by adjusting the mass ratio of SPI and CMC. In addition, the HYD and carboxyl groups were responsive to pH, and therefore, drugs could be rapidly released in an acidic environment. Finally, the insecticidal effect of AVM was found to be reduced after encapsulation with SPI-CMC; however, no significant difference between the insecticidal effect of AVM encapsulate with SPI-CMC and that of the AVM original formulation could be determined. In conclusion, smaller amounts of pesticides could be delivered more efficiently by using the method described in this work, where the release of the resulting encapsulated pesticides can have improved anti-UV properties without affecting the insecticidal effects of the original pesticide. In addition, these materials are more biodegradable than nondegradable materials [52, 53], which protects the environment and promotes the sustainable development of agriculture.

Compliance with ethical standards

Conflict of interest The authors declare that they have no conflict of interest.

Publisher's note: Springer Nature remains neutral with regard to jurisdictional claims in published maps and institutional affiliations.

References

1. Lamberth C, Jeanmart S, Luksch T, Plant A. Current challenges and trends in the discovery of agrochemicals. Science. 2013;341:742–6.
2. Lin G, Zhou H, Lian J, Chen H, Xu H, Zhou X. Preparation of pH-responsive avermectin/feather keratin-hyaluronic acid with anti-UV and sustained-release properties. Colloid Surf B 2019;175:291–9.
3. Huang B, Chen F, Shen Y, Qian K, Wang Y, Sun C, et al. Advances in targeted pesticides with environmentally responsive controlled release by nanotechnology. Nanomaterials. 2018;8:102.
4. Kumar S, Nehra M, Dilbaghi N, Marrazza G, Hassan AA, Kim K. Nano-based smart pesticide formulations emerging opportunities for agriculture. J Control Release. 2019;294:131–53.
5. Reichenberger S, Bach M, Skitschak A, Frede H. Mitigation strategies to reduce pesticide inputs into ground- and surface water and their effectiveness: a review. Sci Total Environ. 2007;384:1–35.
6. Xu C, Cao L, Zhao P, Zhou Z, Cao C, Li F, et al. Emulsion-based synchronous pesticide encapsulation and surface modification of mesoporous silica nanoparticles with carboxymethyl chitosan for controlled azoxystrobin release. Chem Eng J. 2018;348:244–54.
7. Guan H, Chi D, Yu J, Li H. Dynamics of residues from a novel nano-imidacloprid formulation in soyabean fields. Crop Prot. 2010;29:942–6.
8. Wang L, Li X, Zhang G, Dong J, Eastoe J. Oil-in-water nanoemulsions for pesticide formulations. J Colloid Inter Sci 2007;314:230–5.
9. Frederiksen HK, Kristensen HG, Pedersen M. Solid lipid microparticle formulations of the pyrethroid gamma-cyhalothrin—Incompatibility of the lipid and the pyrethroid and biological properties of the formulations. J Control Release. 2003;86:243–52.
10. Zhao X, Cui H, Wang Y, Sun C, Cui B, Zeng Z. Development strategies and prospects of nano-based smart pesticide formulation. J Agr Food Chem 2017;66:6504–12.
11. Zou A, Yang Y, Cheng j, Garamus VM, Li N. Construction and characterization of a novel sustained-release delivery system for hydrophobic pesticides using biodegradable PDA-based microcapsules. J Agr Food Chem. 2018;66:6262–8.
12. Li Y, Zhou M, Pang Y, Qiu X. Lignin-based microsphere: preparation and performance on encapsulating pesticide of avermectin. ACS Sustain Chem Eng. 2017;5:3321–8.

13. Eing M, Olshausen B, Fairfull-Smith KE, Schepers U, Barner-Kowollik C, Blinco JP. Reporting pH-sensitive drug releasevia unpaired spin fluorescence silencing. Polym Chem 2018;9:499–505.

14. Accardo A, Tesauro D, Morelli G. Peptide-based targeting strategies for simultaneous imaging and therapy with nanovectors. Polym J. 2013;45:481–93.

15. Qi P, Bu Y, Xu J, Qin B, Luan S, Song S. PH-responsive release of paclitaxel from hydrazone-containing biodegradable micelles. Colloid Polym Sci. 2017;295:1–12.

16. Jiang T, Li Y, Lv Y, Cheng Y, He F, Zhuo R. Amphiphilic polycarbonate conjugates of doxorubicin with pH-sensitive hydrazone linker for controlled release. Colloid Surf B 2013;111:542–8.

17. Wang L, Wu M, Liu H. Emulsifying and physicochemical properties of soy hull hemicelluloses-soy protein isolate conjugates. Carbohydr Polym 2017;163:181–90.

18. Lin G, Chen X, Zhou H, Zhou X, Xu H, Chen H. Elaboration of a feather keratin/carboxymethyl cellulose complex exhibiting pH sensitivity for sustained pesticide release. J Appl Polym Sci. 2018;136:47160.

19. Alves CR, Ocon P, Avaca LA, Otero TF. Electrodeposition of polypyrrole/carboxymethyl cellulose on platinum and indium tin oxide. Polym J. 2001;33:255–62.

20. Chen N, Lin L, Sun W, Zhao M. Stable and pH-sensitive protein nanogels made by self-assembly of heat denatured soy protein. J Agr Food Chem 2014;62:9553–61.

21. Ying W, Susan S, Donghai W. Effect of esterification on soy protein adhesive performance. T Asabe 2006;49:713–9.

22. Zhang Y, Zhuang X, Gu W, Zhao J. Synthesis of polyacrylonitrile nanoparticles at high monomer concentrations by AIBN-initiated semi-continuous emulsion polymerization method. Eur Polym J. 2015;67:57–65.

23. Chen H, Lin G, Zhou H, Zhou X, Xu H, Huang S. Preparation of avermectin/grafted CMC nanoparticles and their sustained release performance. J Polym Environ. 2018;26:2945–53.

24. Samy W, Elnoby A, El-Gowelli HM, Elgindy N. Hybrid polymeric matrices for oral modified release of desvenlafaxine succinate tablets. Saudi Pharm J 2017;25:676–87.

25. Kholiya F, Chaudhary JP, Vadodariya NG, Meena R. Synthesis of bio-based aldehyde from seaweed polysaccharide and its interaction with bovine serum albumin. Carbohydr Polym 2016;150:278–85.

26. Gong S, Chen H, Zhou X, Gunasekaran S. Synthesis and applications of MANs/poly(MMA-co-BA) nanocomposite latex by miniemulsion polymerization. R Soc Open Sci 2017;4:170844.

27. Yu J, Chang PR, Ma X. The preparation and properties of dialdehyde starch and thermoplastic dialdehyde starch. Carbohydr Polym 2010;79:296–300.

28. Byler DM Jr, Farrell HM. Infrared spectroscopic evidence for calcium ion interaction with carboxylate groups of casein. J Dairy Sci 1989;72:1719–23.

29. He X, He Z, Li Y, Yu H, Zhang L, Ge H, et al. Modeling of the bacterial inactivation kinetics of dialdehyde cellulose in aqueous suspension. Int J Biol Macromol. 2018;116:920–6.

30. Zheng T, Yu X, Pilla S. Mechanical and moisture sensitivity of fully bio-based dialdehyde carboxymethyl cellulose cross-linked soy protein isolate films. Carbohydr Polym 2017;157:1333–40.

31. Jiang X, Yang Z, Peng Y, Han B, Li Z, Li X, et al. Preparation, characterization and feasibility study of dialdehyde carboxymethyl cellulose as a novel crosslinking reagent. Carbohydr Polym 2016;137:632–41.

32. Kosmulski M, Próchniak P, Rosenholm JB. Interaction between surface active solutes and surfaces of metal oxides in polar organic solvents. J Disper Sci Technol. 2010;31:1704–7.

33. Sheng W, Li W, Li B, Li C, Xu Y, Guo X, et al. Mussel-inspired photografting on colloidal spheres: a generalized self-template route to stimuli-responsive hollow spheres for controlled pesticide release. Macromol Rapid Commun 2015;36:1640–5.

34. Cohen S, Haham H, Pellach M, Margel S. Design of UV-absorbing polypropylene films with polymeric benzotriaziole based nano- and microparticle coatings. Acs Appl Mater Inter 2016;9:868–75.

35. Bikova T. UV-absorbance of oxidized xylan and monocarboxyl cellulose in alkaline solutions. Carbohydr Polym 2004;55:315–22.

36. Tabernero A, González-Garcinuño Á, Sánchez-Álvarez JM, Galán MA, Martín Del, Valle EM. Development of a nanoparticle system based on a fructose polymer: stability and drug release studies. Carbohydr Polym 2017;160:26–33.

37. Li Y, Lin J, Yang X, Li Y, Wu S, Huang Y, et al. Self-assembled nanoparticles based on amphiphilic anticancer drug–phospholipid complex for targeted drug delivery and intracellular dual-controlled release. ACS Appl Mater Inter. 2015;7:17573–81.

38. Qi P, Wu X, Liu L, Yu H, Song S. Hydrazone-containing triblock copolymeric micelles for pH-controlled drug delivery. Front Pharmacol 2018;9:12.

39. Moradi A, Abadi ARS, Shahrokhi M. Characterization and kinetics study of the photochlorination of polyethylene. Polym J. 2012;44:973–7.

40. Wu C, An X, Gao S, Su L. Self-assembly of cuprous oxide nanoparticles supported on reduced graphene oxide and their enhanced performance for catalytic reduction of nitrophenols. RSC Adv. 2015;5:71259–67.

41. Shen Z, Zhou H, Chen H, Xu H, Feng C, Zhou X. Synthesis of nano-zinc oxide loaded on mesoporous silica by coordination effect and its photocatalytic degradation property of methyl orange. Nanomaterials 2018;8:317.

42. Lin G, Chen H, Zhou H, Zhou X, Xu H. Preparation of tea tree oil/poly(styrene-butyl methacrylate) microspheres with sustained release and anti-bacterial properties. Materials 2018;11:710.

43. Korsmeyer RW, Gurny R, Doelker E, Buria P, Peppas NA. Mechanisms of solute release from porous hydrophilic polymers. Int J Pharm 1983;15:25–35.

44. Coulibaly FS, Ezoulin MJM, Purohit SS, Ayon NJ, Oyler NA, Youan BC. Layer-by-layer engineered microbicide drug delivery system targeting HIV-1 gp120: physicochemical and biological properties. Mol Pharm 2017;14:3512–27.

45. Zhou H, Shi T, Zhou X. Poly (vinyl alcohol)/SiO2 composite microsphere based on pickering emulsion and its application in controlled drug release. J Biomater Sci Polym Ed. 2014;25:641–56.

46. Haghiralsadat F, Amoabediny G, Helder MN, Naderinezhad S, Sheikhha MH, Forouzanfar T, et al. A comprehensive mathematical model of drug release kinetics from nano-liposomes, derived from optimization studies of cationic PEGylated liposomal doxorubicin formulations for drug-gene delivery. Artif Cell Nanomed B 2018;46:169–77.

47. Chen H, Lin Y, Zhou H, Zhou X, Gong S, Xu H. Synthesis and characterization of chlorpyrifos/copper(II) schiff base mesoporous silica with pH sensitivity for pesticide sustained release. J Agr Food Chem 2016;64:8095–102.

48. Lagorce-Tachon A, Karbowiak T, Simon J, Gougeon R, Bellat J. Diffusion of oxygen through cork stopper: Is it a knudsen or a fickian mechanism? J Agr Food Chem 2014;62:9180–5.

49. Chen H, Lin Y, Zhou H, Zhou X, Gong S, Xu H. Highly efficient alginate sodium encapsulated chlorpyrifos/copper(II) schiff base mesoporous silica sustained release system with pH and ion response for pesticide delivery. RSC Adv. 2016;6:114714–21.

50. Do Nascimento E, de Caland L, de Medeiros A, Fernandes-Pedrosa M, Soares-Sobrinho J, Dos Santos K, et al. Tailoring drug

release properties by gradual changes in the particle engineering of polysaccharide chitosan based powders. Polymer 2017;9:253.

51. Maggio RM, Castellano PM, Kaufman TS. A new principal component analysis-based approach for testing "similarity" of drug dissolution profiles. Eur J Pharm Sci. 2008;34:66–77.

52. Liang J, Yu M, Guo L, Cui B, Zhao X, Sun C, et al. Bioinspired development of P(St–MAA)–avermectin nanoparticles with high

affinity for foliage to enhance folia retention. J Agr Food Chem 2017;66:6578–84.

53. Olejnik A, Nowak I, Schroeder G. Functionalized polystyrene beads as carriers in release studies of two herbicides: 2,4-dichlorophenoxyacetic acid and 2-methyl-4-chlorophenoxyacetic acid. Int J Environ Sci Technol. 2018;1–12. https://doi.org/10.1007/s13762-018-2138-4.